

Adjoint-Based Adaptive Mesh Refinement for Sonic Boom Prediction

Mathias Wintzer*

Stanford University, Stanford, CA 94305

Marian Nemec†

ELORET Corp., Moffett Field, CA 94035

Michael J. Aftosmis‡

NASA Ames Research Center, Moffett Field, CA 94035

Output-driven mesh adaptation is used in conjunction with an embedded-boundary Cartesian meshing scheme for sonic-boom simulations. The approach automatically refines the volume mesh in order to minimize discretization errors in output functionals, specifically pressure signals, defined at locations several body-lengths away from the surface geometry. Techniques and strategies used to improve accuracy of the propagated signal while decreasing mesh densities are described. The effectiveness of this approach is demonstrated in three dimensions using axisymmetric bodies, a lifting wing-body configuration, and the F-5E and Shaped Sonic Boom Demonstration aircraft. Results are validated with available experimental data and indicate that with this approach, accurate pressure signatures can be produced for three-dimensional geometry in just over an hour using a conventional desktop PC.

I. Introduction

OVER the past several years, there has been a renewed interest in supersonic aircraft for civil applications. This resurgence has been partly motivated by significant developments in modeling and simulation, including improved shape optimization capability,¹ novel concepts for supersonic drag reduction,² shape-based boom-tailoring techniques,³ and their validation using a flight demonstrator.⁴ These last two items – critical in that they may lead to a lift of the ban on overland supersonic flight – coupled with a robust business aircraft market, have led to a number of significant design efforts.^{5–7}

When integrating low-boom as a design goal, significant computational resources are required in order to solve the large, dense computational fluid dynamics (CFD) grids needed for high-fidelity sonic-boom prediction. Unlike traditional CFD computations that seek to accurately predict aerodynamic forces, the goal of sonic-boom simulation is to predict, in addition to aerodynamic forces, the pressure distribution at a location several body lengths away from the geometry. These specialized grids are usually constructed by expert users, responsible for estimating what regions of the flow-field influence the accuracy of signal propagation from the complex geometry of the aircraft. CFD analyses performed for the Shaped Sonic Boom Demonstration (SSBD) program illustrate the difficulty of this task.^{8,9} Consequently, lengthy turnaround times make boom constraints difficult to include in a multi-disciplinary design optimization. Overall mission performance may be compromised as design changes are introduced in response to boom predictions which arrive out of phase with the rest of the design cycle.

Several approaches have been investigated to address these issues. These include the use of hand-crafted structured meshes, unstructured meshes with feature-based adaptation,¹⁰ and the use of adjoint-based adaptive procedures on unstructured meshes.¹¹ Our focus is on adjoint-based methods, which are among the most promising approaches for constructing volume meshes that minimize discretization errors in user-selected output functionals. The adjoint approach involves the solution of not only the governing flow equations, but also

*Ph.D. Candidate, Department of Aeronautics and Astronautics; mwintzer@stanford.edu. Member AIAA.

†Research Scientist, Advanced Supercomputing Division, MS T27B; Marian.Nemec@nasa.gov. Member AIAA.

‡Research Scientist, Advanced Supercomputing Division, MS T27B; Michael.Aftosmis@nasa.gov. Senior Member AIAA.

Copyright © 2008 by the American Institute of Aeronautics and Astronautics, Inc. The U.S. Government has a royalty-free license to exercise all rights under the copyright claimed herein for Governmental purposes. All other rights are reserved by the copyright owner.

the corresponding adjoint equations. The adjoint variables weight the residual errors of the flow solution, allowing a direct estimation of the remaining error in output functionals on a given mesh. In our previous work,¹² we have investigated the use of the adjoint approach in conjunction with embedded-boundary Cartesian meshes.¹³ The results show that this combination of accurate error estimates and robust mesh generation yields an automatic and efficient approach for constructing volume meshes in problems with complex geometry. Similar approaches have been proposed by Fidkowski and Darmofal,¹⁴ and Park and Darmofal,¹⁵ but with a focus on embedded-boundary tetrahedral meshes.

The purpose of this work is to extend the use of adjoint-based mesh refinement to the analysis of near-field pressure signals. The present work seeks to automate the construction of meshes that are tailored to effectively minimize the error in the near-field pressure signal while still accurately resolving the traditional aerodynamic coefficients such as lift, drag and pitching moment. In addition to obviating the need to guess where the grid should be manually refined, this automation is shown to reveal subtleties in the flow structure and sensitivities of the near-field pressures which may not be readily apparent to even the expert user. From this near-field signature, the sonic boom at the ground can be rapidly extrapolated using available atmospheric propagation software, such as SBOOM¹⁷ or PCBOOM.¹⁸

The paper begins with a brief overview of adjoint error estimates. Thereafter, we present several techniques, namely grid rotation and cell stretching, and the adaptation strategy we use to obtain affordable meshes for these computations. Three dimensional results are presented for three axisymmetric bodies and a lifting wing-body configuration. We illustrate the effect of accurately capturing body forces on the measured near-field signal for the lifting case. We also show the adaptation time for a typical adaptation process, demonstrating turnaround of highly detailed adaptation simulations in just over an hour on a conventional desktop PC. We compare the accuracy of pressure signals measured on a hand-crafted mesh relative to an adjoint-adapted mesh, demonstrating superior signal quality across the range of refinement levels with substantially fewer grid cells. Finally, the capability of the adaptation method to produce accurate results on actual flight hardware is demonstrated using highly detailed models of the F-5E and SSBD aircraft.

II. Background

The goal of the following derivation is to compute a reliable approximation of a functional $\mathcal{J}(Q)$, such as lift, that is a function of a flow solution $Q = [\rho, \rho u, \rho v, \rho w, \rho E]^T$ satisfying the steady-state three-dimensional Euler equations of a perfect gas

$$\mathcal{F}(Q) = 0 \quad (1)$$

Let $J(\mathbf{Q}_H)$ denote an approximation of the functional computed on an affordable Cartesian mesh with a characteristic cell size H , where $\mathbf{Q} = [\bar{Q}_1, \bar{Q}_2, \dots, \bar{Q}_N]^T$ is the discrete solution vector of the cell-averaged values for all N cells of the mesh and J is the discrete operator used to evaluate the functional. The governing equations are discretized on a multilevel Cartesian mesh with embedded boundaries. The mesh consists of regular Cartesian hexahedra everywhere, except for a layer of body-intersecting cells, or *cut-cells*, adjacent to the boundaries as illustrated in Fig. 1. The spatial discretization of Eq. 1 uses a cell-centered, second-order accurate finite volume method with a weak imposition of boundary conditions, resulting in a system of equations

$$\mathbf{R}(\mathbf{Q}_H) = 0 \quad (2)$$

The flux-vector splitting approach of van Leer¹⁹ is used. The mesh is viewed as an unstructured collection of control volumes, which makes this approach well-suited for solution-adaptive mesh refinement. Steady-state flow solutions are obtained using a five-stage Runge–Kutta scheme with local time stepping, multigrid, and a domain decomposition scheme for parallel computing; for more details see Aftosmis *et al.*^{20,21} and Berger *et al.*²²

To approximate the functional error $|\mathcal{J}(Q) - J(\mathbf{Q}_H)|$, we consider isotropic refinement of an initial Cartesian mesh to obtain a finer mesh with average cell size h containing approximately $8N$ cells (in three dimensions), and seek to compute the discrete error $|J(\mathbf{Q}_h) - J(\mathbf{Q}_H)|$ without solving the problem on the embedded, fine mesh. Our approach follows the work of Venditti and Darmofal,²³ where Taylor series

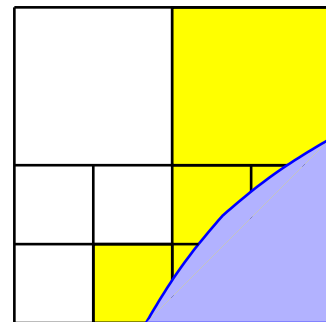


Figure 1. Multilevel Cartesian mesh in two-dimensions with a cut-cell boundary

expansions of the functional and residual equations are used on the embedded mesh about the coarse mesh solution. The result is an estimate of the functional on the embedded mesh, given by

$$J(\mathbf{Q}_h) \approx J(\mathbf{Q}_h^H) - \underbrace{(\psi_h^H)^T \mathbf{R}(\mathbf{Q}_h^H)}_{\text{Adjoint Correction}} - \underbrace{(\psi_h - \psi_h^H)^T \mathbf{R}(\mathbf{Q}_h^H)}_{\text{Remaining Error}} \quad (3)$$

where \mathbf{Q}_h^H and ψ_h^H denote a reconstruction of the flow and adjoint variables from the coarse mesh to the embedded mesh, and the adjoint variables satisfy the following linear system of equations

$$\left[\frac{\partial \mathbf{R}(\mathbf{Q}_H)}{\partial \mathbf{Q}_H} \right]^T \psi_H = \frac{\partial J(\mathbf{Q}_H)}{\partial \mathbf{Q}_H}^T \quad (4)$$

Ref. 24 gives details on the implementation of the adjoint solver.

Referring to Eq. 3, the adjoint variables provide a correction term that improves the accuracy of the functional on the coarse mesh, and a remaining error term that is used to form an error-bound estimate and a localized refinement parameter. A difficulty with the remaining error term is that it depends on the solution of the adjoint equation on the embedded mesh, ψ_h . We approximate ψ_h with an interpolated adjoint solution from the coarse mesh. A piecewise linear and constant reconstruction is used, and the details of this approximation are presented in Ref. 25. The advantages of this approach are robustness, especially in regions where the flow and adjoint solutions exhibit steep gradients and discontinuities, and simplicity of implementation. The disadvantage is a reduction in accuracy of the adjoint correction and remaining error terms. Ongoing work is focused on the use of higher-order interpolation to improve the accuracy of these terms. The remaining error term in Eq. 3 is used to estimate a bound on the local error in each cell k of the coarse mesh

$$e_k = \sum \left| (\psi_L - \psi_C)^T \mathbf{R}(Q_L) \right|_k \quad (5)$$

where the sum is performed over the children of each coarse cell, and subscripts $(\cdot)_L$ and $(\cdot)_C$ denote piecewise linear and constant reconstruction, respectively. An estimate of the net functional error E is the sum of the cell-wise error contributions to the functional

$$E = \sum_{k=0}^N e_k \quad (6)$$

Given a user-specified global tolerance TOL for the functional of interest, the termination criterion for the simulation is satisfied when

$$E \leq \text{TOL} \quad (7)$$

To define a local refinement parameter on the coarse mesh, we specify a maximum allowable error level, t , for each cell by equidistributing the user-specified tolerance over the cells of the coarse mesh

$$t = \frac{\text{TOL}}{N} \quad (8)$$

The refinement parameter, r_k , is given by

$$r_k = \frac{e_k}{t} \quad (9)$$

which is the ratio of the cell-wise error, given by Eq. 5, to the maximum allowable error. A cell is flagged for refinement if

$$r_k > \lambda \quad (10)$$

where $\lambda \geq 1$ is a global *refinement threshold* chosen by various adaptation strategies, which are described in Ref. 12 and further discussed below. The refinement parameter drives an incremental adaptation strategy. Starting from a coarse initial mesh, cells are flagged for refinement as indicated by Eq. 10. The solution is computed on the refined mesh and the adaptation cycles continue until the termination criterion is satisfied. The refinement region is typically enlarged by one coarse cell to ensure that the interface boundary of the refined region of the mesh is in a region of low error.

III. Techniques and Strategy

III.A. Grid Rotation and Cell Aspect Ratio

In Ref. 12, we used a model two-dimensional problem to demonstrate the effectiveness of grid rotation and increased cell aspect ratio (“cell stretching”) to improve propagation of signals through a multi-level Cartesian mesh. The grid is rotated to roughly align mesh cells with the freestream Mach-wave angle, similar to Ref. 8. To avoid the well-known “sonic-glitch”,²⁶ the mesh is rotated slightly away from the Mach-wave angle of the freestream flow. For cases presented in this work, the deviation is about 3° . Furthermore, mesh cells are stretched along the dominant wave direction to directly increase the per-cell signal propagation distance. We also introduced a quadratic form of the field functional

$$J_s = \int_0^L \left(\frac{\Delta p}{p_\infty} \right)^2 ds \quad (11)$$

where L is the sensor length, and $\Delta p = p - p_\infty$. This functional form focuses cell refinement around regions of rapid pressure change, resulting in more efficient adapted meshes with improved signal accuracy. Taken together, these techniques yielded an order of magnitude reduction in adapted cell counts relative to an isotropic, Cartesian-aligned grid using a linear target functional.

III.B. Adaptation Strategy

We use two heuristics to fine-tune the adaptation procedure. The first allows control over the maximum refinement level in the new mesh. While one level of refinement is typically allowed at each adaptation cycle, experience with field functionals shows additional benefits from adaptation cycles where the maximum refinement level is held fixed. These “propagation only” adaptation sweeps move refinement interfaces to regions of low error and are very affordable since they add relatively few new cells. The second heuristic allows specification of the threshold λ in Eq. 10 for each adaptation cycle. We use the expected convergence rate of the functional and statistical analysis of error distribution on the coarse mesh to determine a sequence of thresholds that reduce the run-time of the simulation and improve accuracy.

In Ref. 12, we outlined a decreasing threshold, or “worst things first” approach to control mesh growth through the adaptation process. This approach was shown to improve process efficiency by targeting only the highest error cells for refinement during early adaptation cycles. We find for the off-body pressure functional that actively adjusting both heuristics in response to statistics measured on the previous mesh prevents excessive mesh growth and can greatly improve the quality of the propagated signal.

In this adaptive threshold strategy, we set the value of λ during a given cycle to meet a specific cell growth target. During early adaptations where flow and adjoint solution accuracy is limited by mesh coarseness, this target may be as small as 5%, but is allowed to increase to 100% as the mesh refinement level increases. We also monitor the refinement level of targeted cells, and hold the maximum refinement level steady if the majority of these cells is found to be at a lower level of refinement. By restricting increases in refinement in this fashion, cell growth is tightly controlled, and mesh interfaces are aggressively propagated outside the region of influence.

IV. Results

IV.A. Axisymmetric Body

A simple axisymmetric body is selected to illustrate the effectiveness of these techniques in three dimensions. This first case is also used as a validation case in Refs. 10 and 11, and reproduces the stepped cone form (referred to as “Model 8”, see Fig. 2) described in a 1965 wind tunnel study.²⁷ As in Ref. 11, the nose of the geometry is given a 0.003 inch radius.

As illustrated in Fig. 3(a), the body is placed at 0° angle of attack in Mach 1.26 freestream flow, with its nose at the origin. The pressure sensor has an offset distance h/l of 6

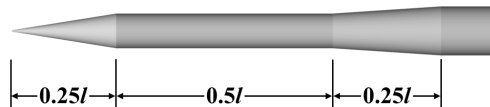


Figure 2. Model 8 geometry, from Ref. 27

body-lengths, placing it 8 units behind and 12 units above the origin, aligned with the freestream. The far-field boundaries are located 60 units away from the body, and a symmetry plane is placed at $z = 0$.

We first consider a grid consisting of isotropic cells. The initial mesh is depicted in Fig. 3(a), and contains 11,855 cells. Only 7 grid cells span the length of the body. An error tolerance of 10^{-6} is used. Adaptation is performed until the maximum mesh refinement level has increased by 4, and takes 20 cycles in total. The final mesh, shown in Fig. 3(b), contains just under 19 million cells. Mesh refinement is focused about shocks, and the regions of influence below the body and above the sensor. Pressure contours (Fig. 3(c)) show, qualitatively, the shock interactions that reduce the complex pressure patterns at the body surface to the relatively simple double N-wave shown in Fig. 3(d). The adapted near-field pressure signal, with 394 points along the sensor, shows good agreement with wind tunnel data (Ref. 27). Convergence of the functional and its error estimate are shown in Figs. 3(e) and (f), respectively. The corrected functional accurately predicts the functional value on the last few refinement cycles, though neither appears fully converged.

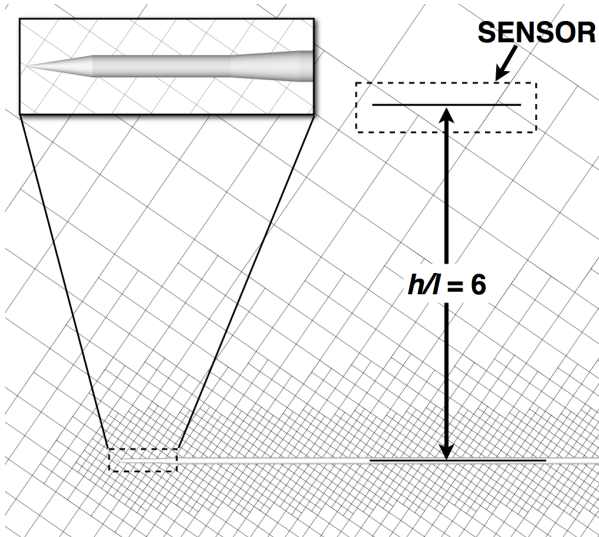
The initial bunching of points in Figs. 3(e) and (f) is characteristic of the adaptive threshold strategy, where the restrictive refinement rules limit cell growth. This can be explained by considering that cell refinement on the initial mesh is driven purely by geometric features of the surface triangulation. This leads to rapid coarsening of the mesh between the body and the sensor, and results in the low initial error values. The situation is quickly remedied after several propagation passes, at which point the accuracy of the adjoint error estimator improves, and more sources of signal error can be resolved. The peak in the curve is simply the point where mesh quality and error estimate accuracy are sufficient to overcome initial grid bias and enable progress towards lower levels of global error.

To further explore this insight, we consider a grid with a cell aspect ratio (AR) of 4. The mesh is stretched in all but the wave-normal direction, such that the resulting volume grid cells are tile-shaped. The problem setup is otherwise identical to the isotropic case. The 11,489 cell initial mesh is shown in Fig. 4(a). As for the isotropic case, adaptation is performed until the maximum mesh refinement level has increased by 4, and takes 12 cycles in total. The final mesh is shown in Fig. 4(b), and contains only 5.1 million cells – a factor of 4 reduction in cell count over the isotropic case. While displaying similar characteristics to the isotropic cell mesh, it is visibly more sparse, with pronounced thinning of the grid in expansion regions, and tighter clustering of cells about shocks. Pressure contours for the stretched mesh (Fig. 4(c)) differ from the isotropic mesh only in the region beneath the body, where the pressure waves dissipate more rapidly into less refined regions of the mesh. The pressure signal, with 449 points along the sensor, again shows good agreement with wind tunnel data (Fig. 4(d)). When compared to the isotropic case, the superior signal-propagating properties of the stretched mesh are evident in the higher magnitudes and qualitatively more recognizable pressure signals predicted at the lower refinement levels. Functional convergence (Fig. 4(e)) is substantially more convincing than for the isotropic case, and appears to be asymptotic over the final two adaptation cycles. The error estimate curve is shown in Fig. 4(f). The initial error rise is steeper than for the isotropic case, suggesting a more efficient process of initial error propagation.

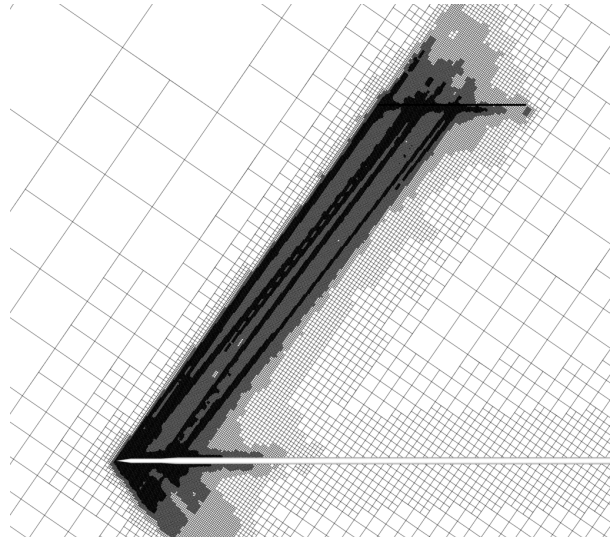
Figure 5(a) directly compares the error estimate change with cell count for the isotropic and stretched-cell cases. The latter reaches a level of error similar to that of the isotropic cell case with almost an order of magnitude fewer cells. When closely comparing the pressure signals produced by each type of mesh (Fig. 5(b)), we further note that at a similar level of error, the stretched mesh is able to produce a more crisp signal.

Additional cases further illustrate the adaptation capability at higher Mach numbers and offset distances. Figures 6(a) and (b) show pressure signals predicted using the present flow conditions, but at $h/l = 10$ and $h/l = 18$, respectively. Figures 6(c) and (d) place the sensor at $h/l = 10$, with freestream flow at Mach 1.41 and Mach 2.01, respectively. In all cases, agreement with wind tunnel data is good.

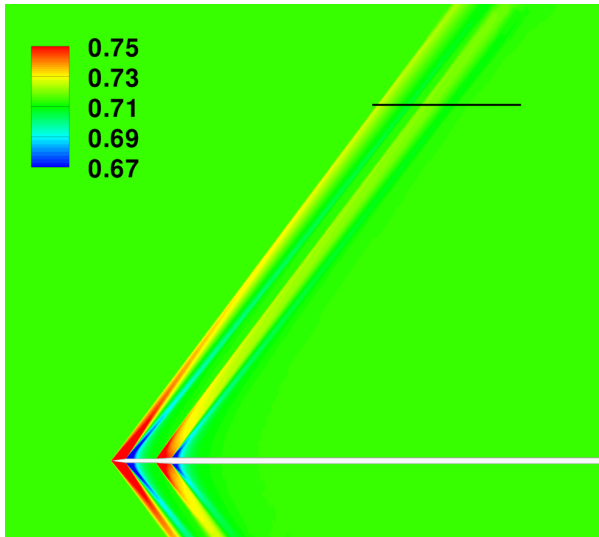
To this point, all signals shown are of a simple N-wave form. Two additional axisymmetric body shapes are selected from Ref. 27 to demonstrate that the adaptation is fundamentally able to capture signal forms that are of interest in low-boom design. The Model 1 geometry, shown in Fig. 7(a), generates a weak bow shock due to its small cone half-angle of 3.23° . The Model 2 geometry, shown in Fig. 7(b), produces a rooftop-shaped signal due to its cone half-angle of 6.46° . Pressure signals predicted for each geometry in a freestream flow of Mach 1.41 and with sensor offset of $h/l = 5$ are shown in Figs. 7(c) and (d). Agreement with wind tunnel data is good, matching both the shock-free and rooftop signal forms for Model 1 and Model 2, respectively, on very affordable meshes containing roughly 4 million cells.



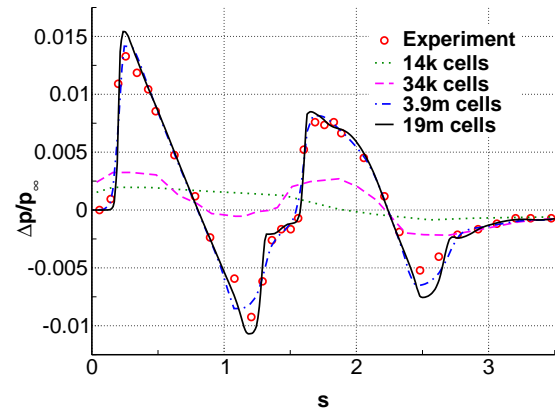
(a) Initial mesh; 12k cells



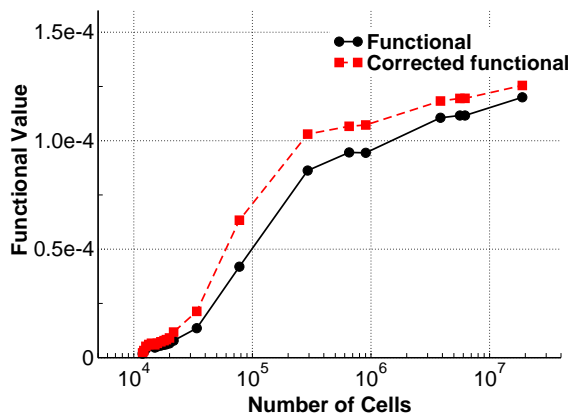
(b) Final mesh; 19M cells



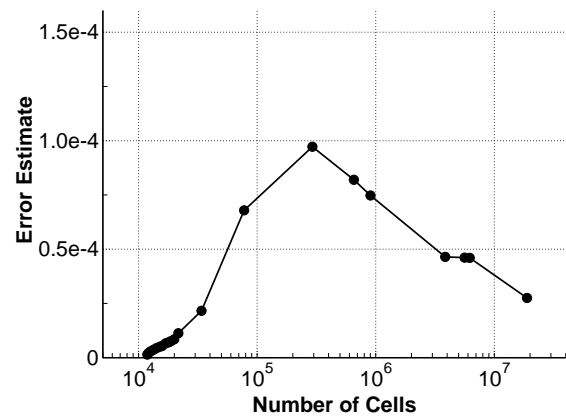
(c) Pressure contours on final mesh; 394 points along sensor



(d) Pressure signals measured after each refinement pass

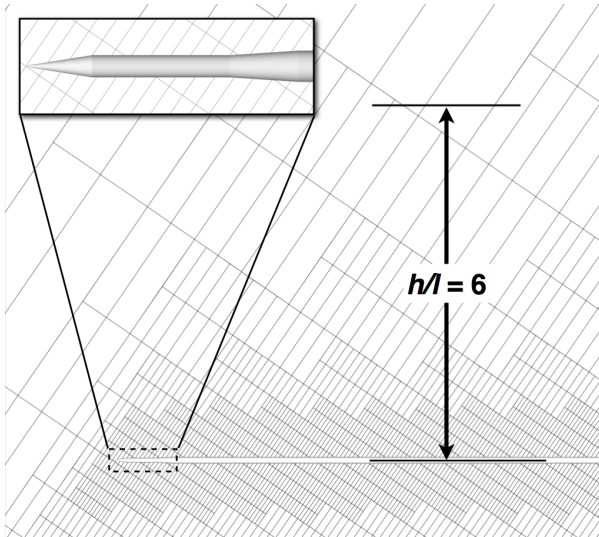


(e) Convergence of functional

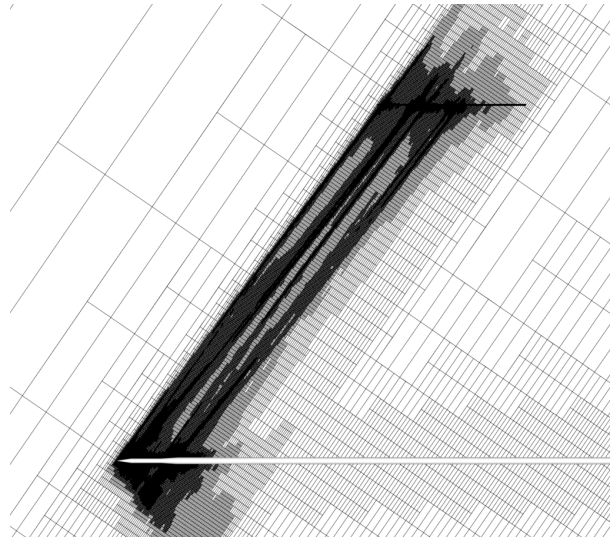


(f) Error estimate

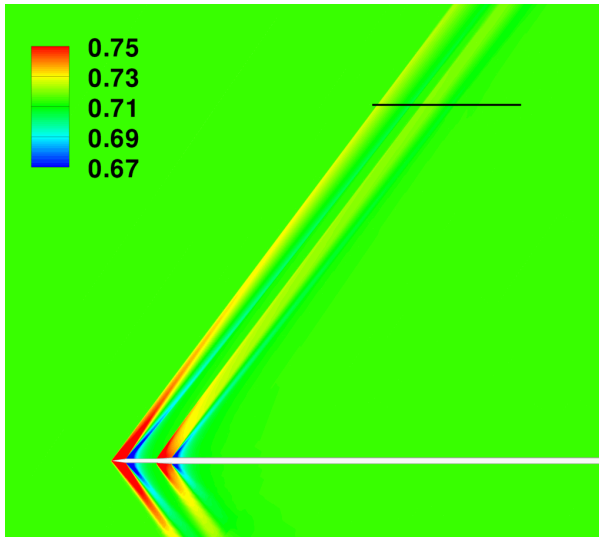
Figure 3. Summarized results of adjoint-driven refinement on isotropic ($AR = 1$) mesh for Model 8 axisymmetric body. $M_\infty = 1.26$, $\alpha = 0$ and $h/l = 6$. Experimental data from Ref. 27



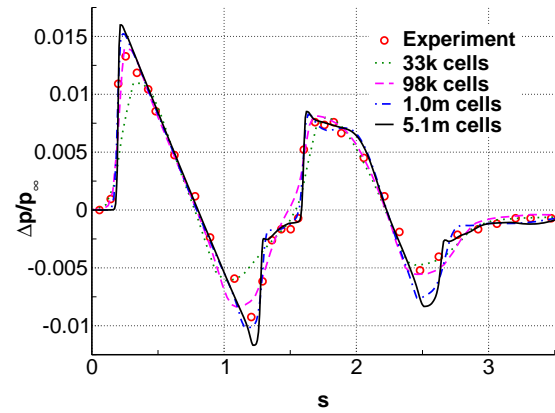
(a) Initial mesh; 11k cells



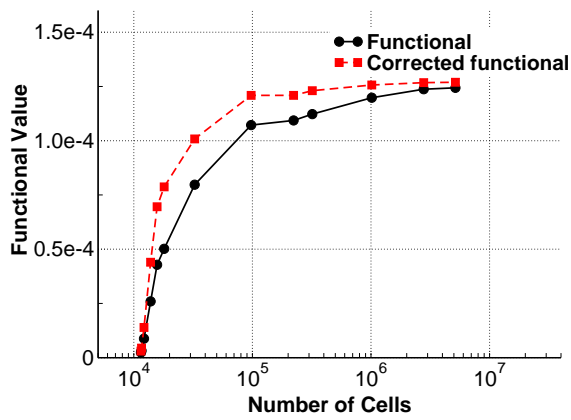
(b) Final mesh; 5.1M cells



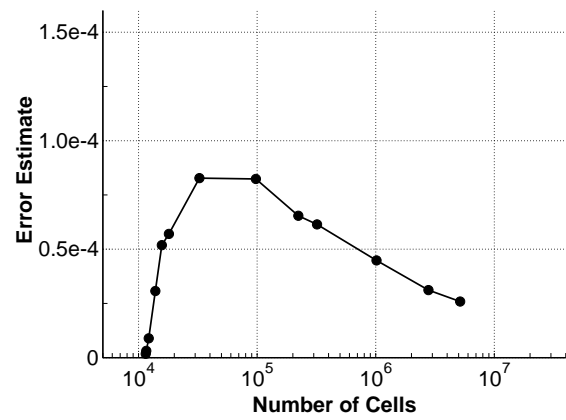
(c) Pressure contours on final mesh; 449 points along sensor



(d) Pressure signals measured after each refinement pass

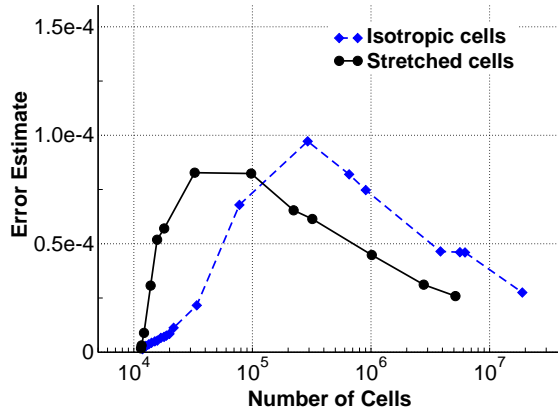


(e) Convergence of functional

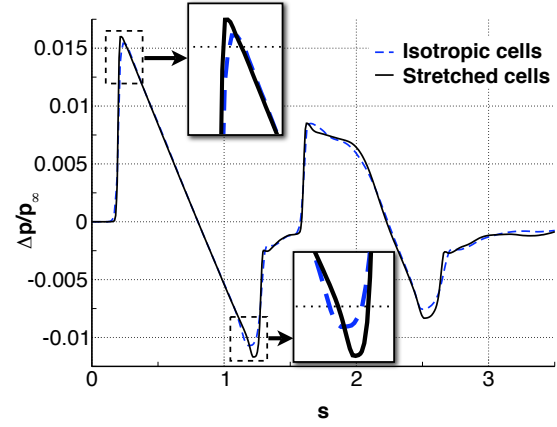


(f) Error estimate

Figure 4. Summarized results of adjoint-driven refinement on stretched ($AR = 4$) mesh for Model 8 axisymmetric body. $M_\infty = 1.26$, $\alpha = 0$, and $h/l = 6$. Experimental data from Ref. 27

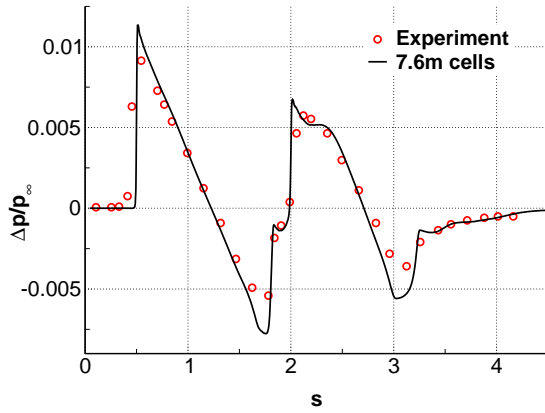


(a) Error estimates

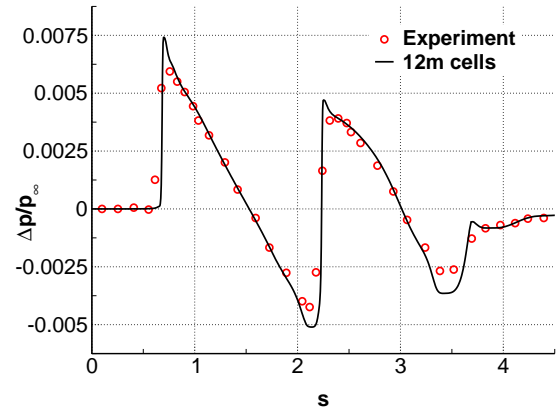


(b) Pressure signals; $M_\infty = 1.26$, $\alpha = 0$, $h/l = 6$

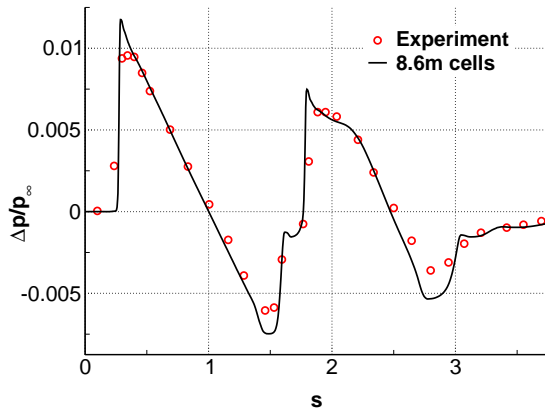
Figure 5. Comparison of final results for Model 8 axisymmetric body with isotropic ($AR = 1$) and stretched ($AR = 4$) cells



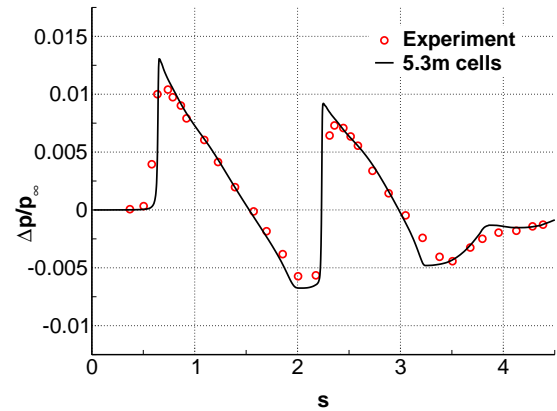
(a) $M_\infty = 1.26$, $h/l = 10$; 568 points along sensor



(b) $M_\infty = 1.26$, $h/l = 18$; 562 points along sensor



(c) $M_\infty = 1.41$, $h/l = 10$; 602 points along sensor



(d) $M_\infty = 2.01$, $h/l = 10$; 507 points along sensor

Figure 6. Pressure signals at additional Mach numbers and sensor offset distances for Model 8 axisymmetric body. Experimental data from Ref. 27

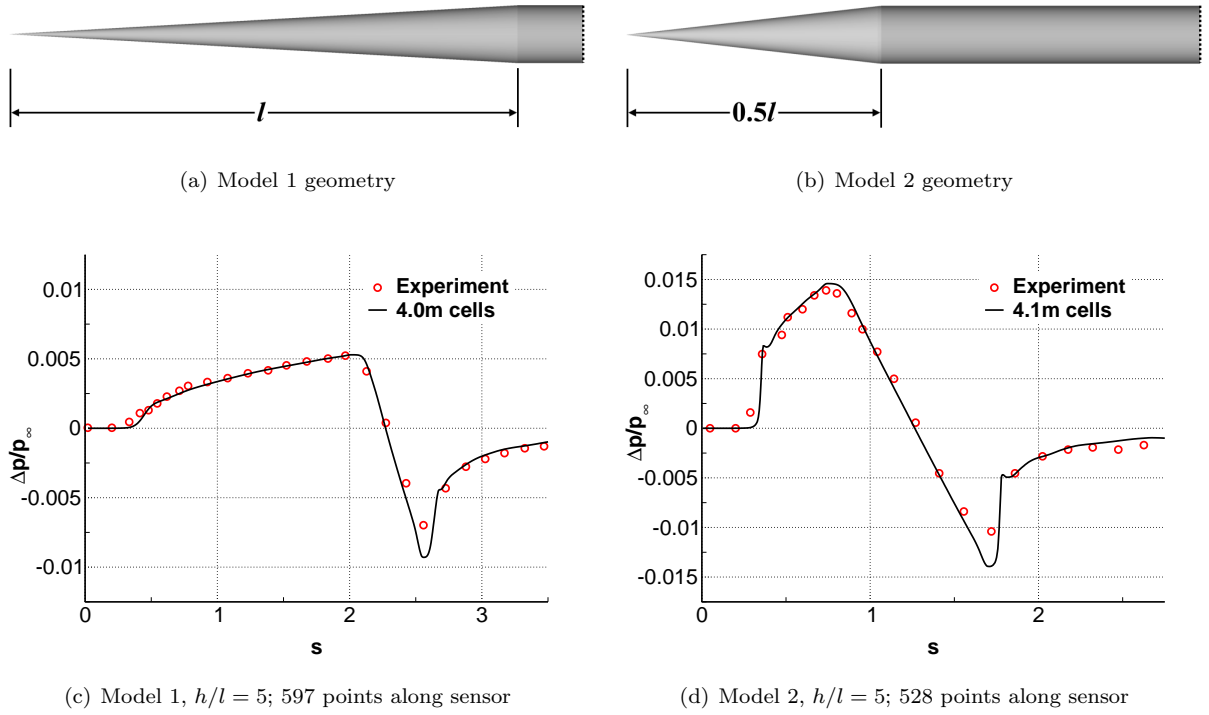


Figure 7. Shock-free and rooftop pressure signals recorded at Mach 1.41 freestream conditions for Model 1 and Model 2 axisymmetric bodies, respectively. Experimental data from Ref. 27

IV.B. Lifting Wing-Body

We now consider a wing-body geometry to validate the current approach on a lifting configuration. The “Model 4” geometry described in a 1973 wind tunnel study²⁸ is selected. Model 4 was also selected for study in Refs. 15 and 29. This geometry consists of an axisymmetric fuselage with a 69° leading edge sweep delta wing (Fig. 8). The air-foil is a symmetric, 5% thick diamond section. The Computational Analysis PROGRAMming Interface (CAPRI)³⁰ is used to generate a watertight surface triangulation from an existing CAD model. Reference 28 gives no dimensions for the sting, providing only a photograph of the model mounted in the wind tunnel, and a sketch of the wind-tunnel apparatus. Based on this limited data, we roughly approximate the sting as a simple body of revolution meeting the base of the model at a stepped junction, and extending 4 body-lengths behind the geometry.

The angle of attack was set to match the desired lift coefficient (C_L) of 0.08. The nose of the geometry is placed at the origin, and the pressure sensor is defined parallel to the freestream at $h/l = 3.6$. The volume grid is rotated 39.5° relative to the Cartesian axes. The far-field boundaries are located 300 units from the body, and a symmetry plane is placed at $z = 0$. The grid is stretched along the y and z coordinate directions to produce tile-shaped, $AR = 4$ grid cells. An error tolerance of 10^{-3} is used.

The initial mesh is depicted in Fig. 9(a), and contains 22,453 cells. Adaptation is performed until the maximum mesh refinement level has increased by 4, and takes 15 cycles. The final mesh, shown in Fig. 9(b), contains just under 4.1 million cells. Cells are concentrated around shocks, with the bow, lift-induced and aft shocks being clearly defined starting roughly one body-length beneath the geometry. The pressure contour

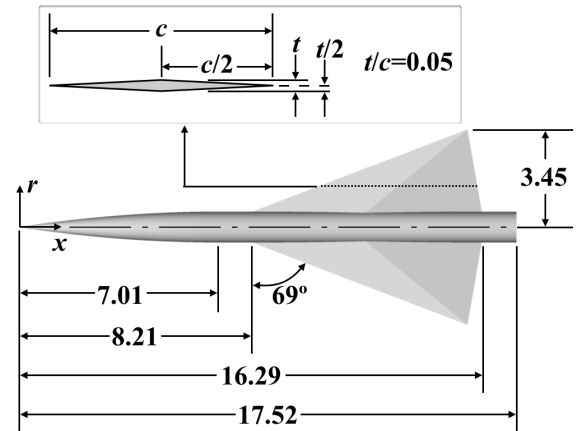


Figure 8. Model 4 delta-wing-body geometry, from Ref 28

plot in Fig. 9(c) shows the compression and expansion regions around the wing which contribute the strong second shock observed in the pressure signal plot (Fig. 9(d)). The signal predicted by the final adapted mesh contains 498 points along the sensor, and shows good agreement with the wind tunnel data. We attribute the difference between adapted and experimental results between $s = 19$ and $s = 21$ to be due to the inaccurate representation of the body-sting junction. While some effort was spent in Ref. 29 to generate a sting geometry that matched the aft shock more accurately, it is only valid at the zero lift condition, and is thus not applicable to the lifting case presented here. Convergence of the functional is shown in Fig. 9(e), and appears to be approaching an asymptote over the final 4 adaptation cycles. The error estimate curve in Fig. 9(f) shows the characteristic rise and fall pattern observed in the Model 8 results.

IV.B.1. Simultaneous Adaptation to Body Force and Field Functional

A lifting wing-body generates a flowfield disturbance in proportion to the degree of lift generated. The accuracy with which this disturbance is captured affects the character of the propagated signal. Cell-stretching reduces the effective surface resolution, in turn degrading the accuracy with which integrated body forces are predicted. We seek to determine the effect of reduced body force error on the predicted off-body pressure signal. By augmenting the target functional to include normal and axial body forces, the adaptation objective function J becomes a linear combination of the body force functionals J_{C_N} and J_{C_A} , and the pressure sensor functional J_s defined in Eq. 11

$$J = W_1 J_{C_N} + W_2 J_{C_A} + W_3 J_s \quad (12)$$

where W_1 , W_2 and W_3 are weighting factors that default to 1. We set $W_3 = 10$ so that the error contribution from the sensor functional is comparable to that of the body force functional.

Adaptations using this augmented functional are performed both for the stretched mesh, and for an isotropic mesh using the same simulation conditions. The final stretched mesh contains 5.1 million cells; for comparison purposes we tune the isotropic mesh adaptation to produce a similar number of cells. The estimated error in the predicted body forces is compared in Fig. 10(a) for the baseline stretched mesh case without body forces, and for the stretched and isotropic cases with the augmented functional. The error decreases most rapidly for the isotropic cell case, though error levels for all three cases are comparable by the final adaptation cycle. Between the two stretched mesh results, the augmented functional adaptation gives slightly less error at a given cell count. The estimated error in the pressure functional (Fig. 10(b)) shows the isotropic mesh case with the highest terminal error, as expected. Disregarding slight differences early in the adaptation, the stretched mesh errors are essentially identical.

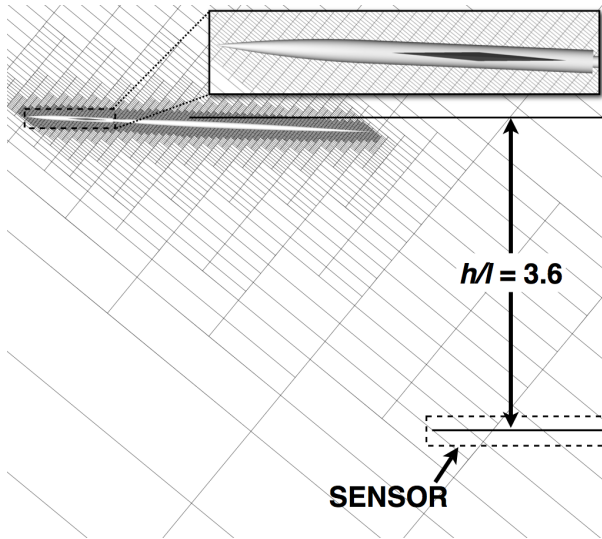
Comparing the final meshes for the baseline and augmented cases shows qualitatively similar refinement structure everywhere except in the near-body region, where the augmented functional mesh has higher cell density. Taken in the context of these error trends, one hypothesis is that the additional cells on the augmented mesh primarily exist to improve prediction of the integrated body forces. As such, the cost of including body forces is not a percentage of the baseline cell count, but a fixed value. While not immediately apparent for this simple geometry, the assurance that mesh refinement is appropriate for both prediction of the near-field signal, as well as integrated body forces, seems worth the slight increase in time and resources when using the augmented functional form.

To illustrate the intricate refinement structure typically produced by the adaptation, the near-body grid for the augmented functional, stretched mesh is shown in Fig. 11. Two slices through the volume grid are shown; one at the symmetry plane, and one at $z = 2$. Only cells at the 3 highest levels of refinement are drawn. Note the increased refinement around the bow shock visible in both cut planes. For this lifting case, we also observe additional refinement along the stagnation line approaching the wing leading edge.

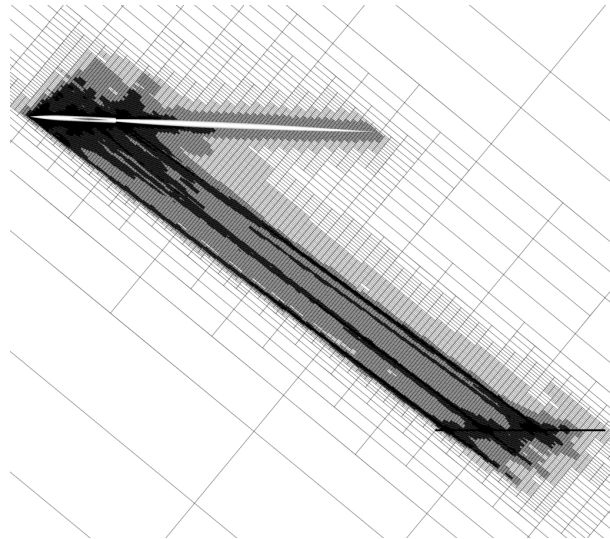
The two additional lift conditions for Mach 1.68 flow presented in Ref. 28 are now considered. The augmented functional described in Eq. 12 is used for each adaptation. Figures 12(a) and (b) show the pressure signals predicted for the $C_L = 0$ and $C_L = 0.15$ conditions, respectively. In both cases, agreement with wind tunnel data is good. We note that at these lift conditions, the trailing artifact present in the signal predicted at $C_L = 0.08$ does not appear.

IV.B.2. Typical Run Timing

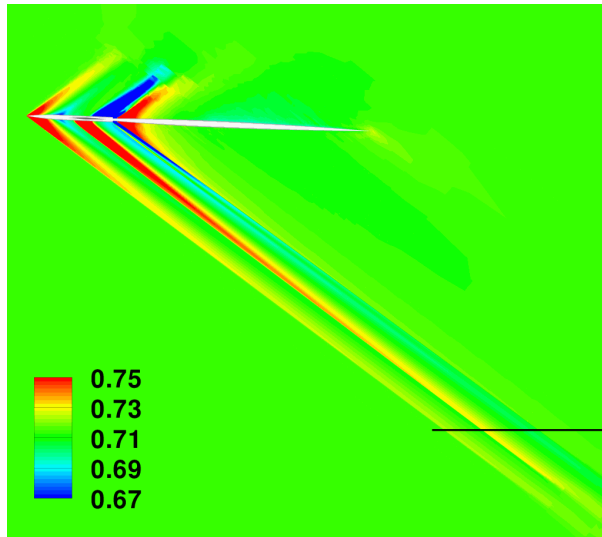
The pie chart shown in Fig. 13 offers some insight into the wall-clock time required by each subprocess in this mesh adaptation. For this example, we use the stretched grid case with augmented functional, containing



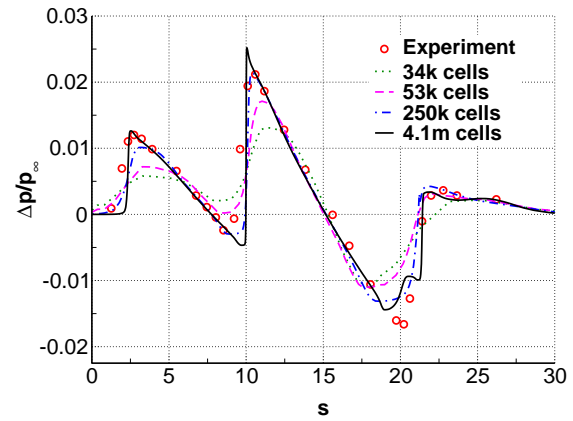
(a) Initial mesh; 22k cells



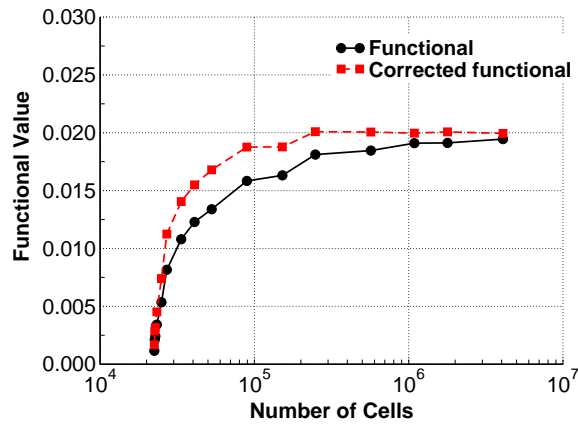
(b) Final mesh; 4.1M cells



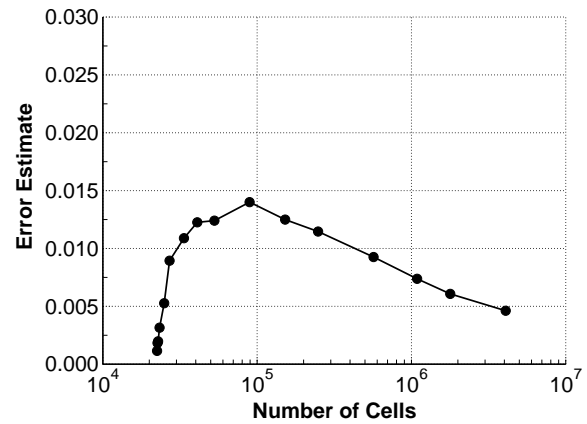
(c) Pressure contours on final mesh; 498 points along sensor



(d) Pressure signals measured after each refinement pass

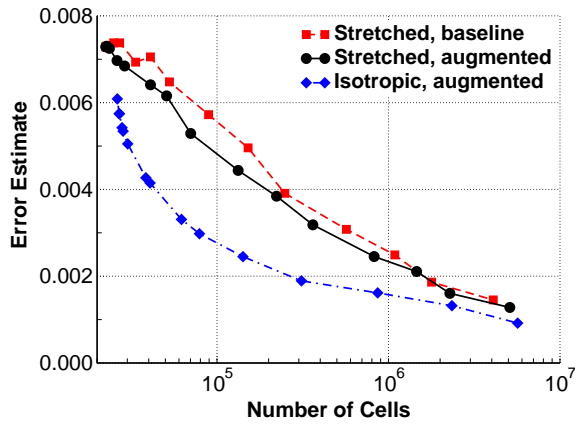


(e) Convergence of functional

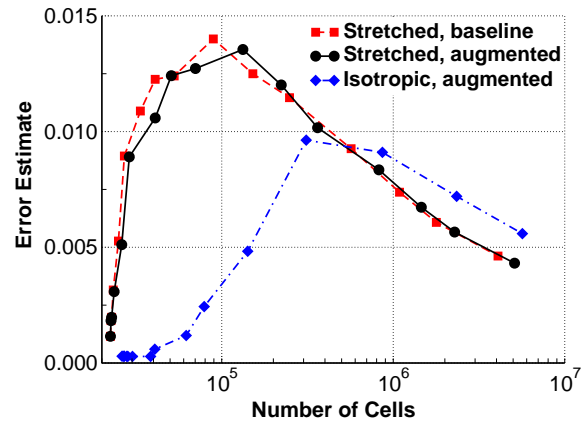


(f) Error estimate

Figure 9. Summarized results of adjoint-driven mesh refinement on $AR = 4$ mesh for Model 4 lifting-wing-body; adapting to minimize sensor errors only. $M_\infty = 1.68$, $C_L = 0.08$, and $h/l = 3.6$. Experimental data from Ref. 28



(a) Error estimates for body force functional



(b) Error estimates for pressure functional

Figure 10. Comparison of body force and pressure functional error estimates for the baseline, augmented stretched ($AR = 4$) and augmented isotropic ($AR = 1$) cases; note different ordinate scales. Baseline mesh contains 4.1 million cells, while augmented functional grids both contain roughly 5 million cells

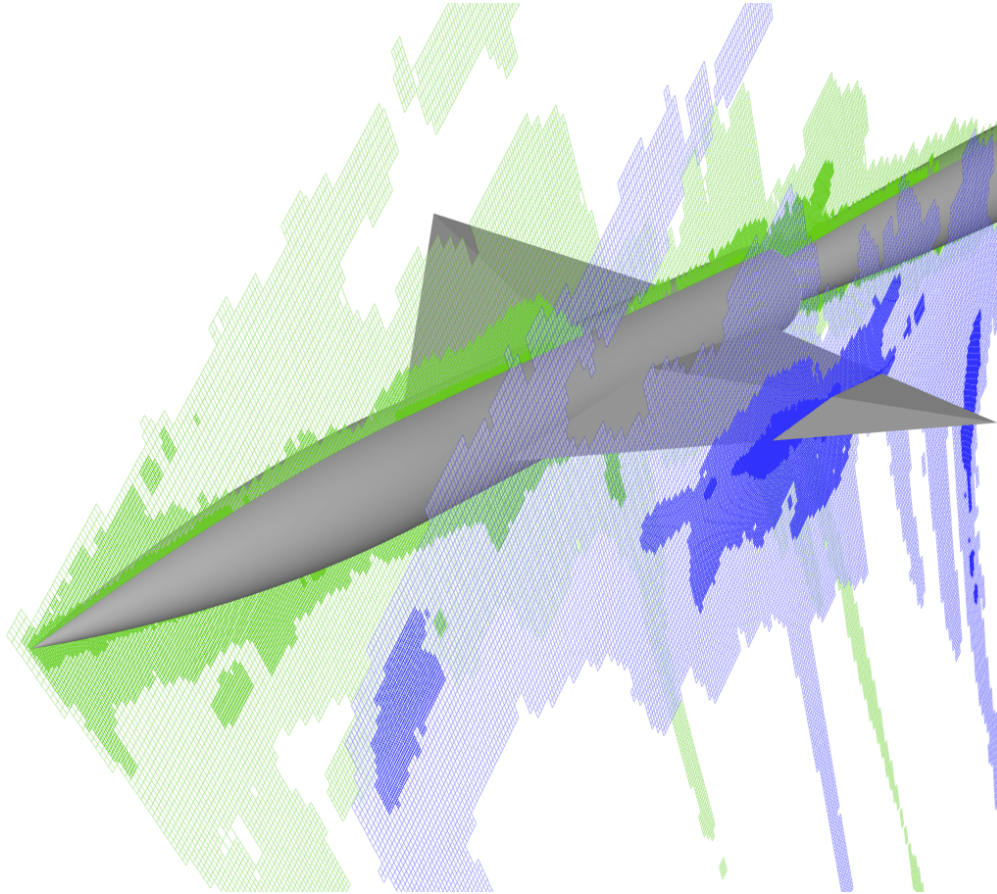


Figure 11. Final mesh near body following adaptation with augmented functional; mesh slices taken at $z = 0$ (green) and $z = 2$ (blue); $M_\infty = 1.68$, $C_L = 0.08$, 5.1 million total grid cells

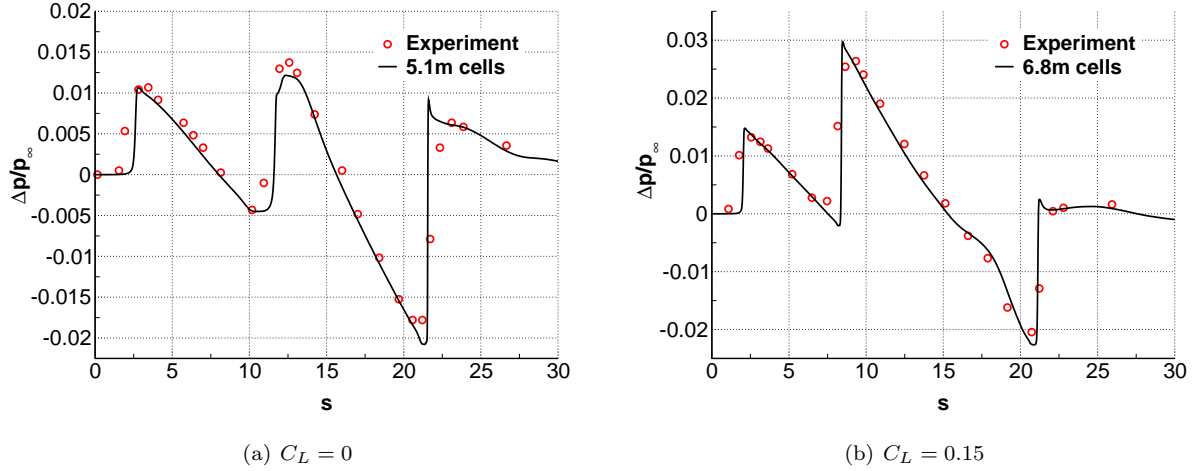


Figure 12. Pressure signals at various lift conditions for Model 4 lifting-wing-body geometry in $M_\infty = 1.68$ flow. Experimental data from Ref. 28

5.1 million cells in the final mesh after 15 adapt cycles, and with a surface discretization for the wing-body geometry consisting of 1.3 million triangles. The case is run on an 8-core desktop PC^a. Values shown are minutes of wall-clock time consumed by each subprocess over the entire adaptation. The mesh adaptation on this wing-body geometry totaled 1 hour and 21 minutes. The timing breakdown is typical, with roughly two-thirds of the time dedicated to the flow solver, and the other one-third to adaptation mechanics. Note that the flow solution on the final mesh takes 28 minutes – roughly half the total flow solving time, and one third of the total adaptation time.

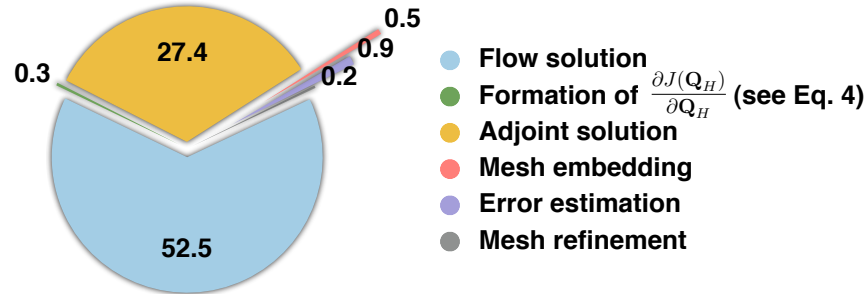
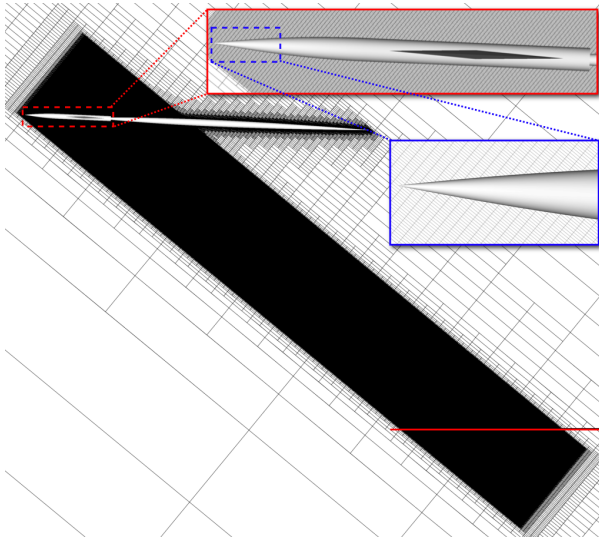


Figure 13. Chart showing time consumed (in minutes) by each subprocess of the adaptation for the $C_L = 0.08$, stretched grid case with augmented functional. Final mesh contains 5.1M cells after 15 adapt cycles. Total time for this case was 1 hour, 21 minutes on an 8-core desktop PC

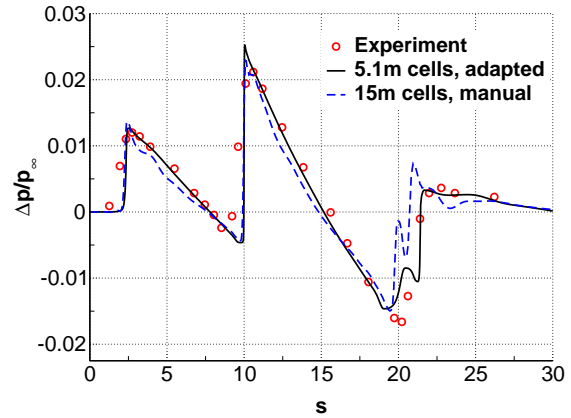
IV.B.3. Comparison with Manually Defined Mesh

Finally, we compare the performance of manually refined and adjoint adapted volume grids. To generate the manual grid shown in Fig. 14(a), we define an extruded rectangular region enclosing the wing, body and off-body sensor and specify its refinement level. The highest level usable was 11, with higher refinement levels resulting in impractically large cell counts. The comparison is arguably weighted in favor of the manually-refined grid in that we know beforehand the extent of the signal along the sensor from the adjoint adapted result, and can thus size the refinement box appropriately. Despite this, the predicted pressure signal on the manual grid (Fig. 14(b)) is qualitatively poor, with visible artifacts in the expansion regions of the signal. The estimated error for the augmented functional is evaluated on manual grids at refinement levels of 8, 9, 10 and 11, and compared with the equivalent adapted mesh result in Fig. 14(c). In this case, the manually refined mesh required 2 orders of magnitude more cells to reach levels of error similar to that of the adapted mesh.

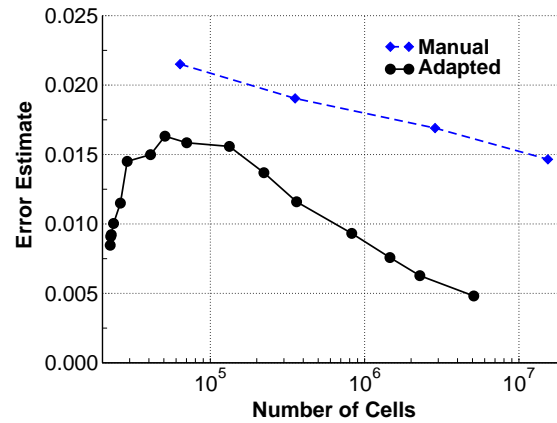
^aA dual-quad (8 cores) 3.2 GHz Intel Xeon PC



(a) Manual mesh; maximum refinement level 11, 15m cells



(b) Pressure signal comparison; 15m cell manual mesh, 5.1m cell adapted mesh with maximum refinement level 13



(c) Mesh error estimates using manual mesh refinement and output-based adaptation with augmented functional

Figure 14. Comparison of results obtained with manually defined and adapted meshes for Model 4 wing-body geometry in $M_\infty = 1.68$ flow at $C_L = 0.08$. Experimental data from Ref. 28

IV.C. F-5E and Shaped Sonic Boom Demonstration Aircraft

This final case demonstrates the capability of the proposed mesh adaptation approach when applied to real-world configurations. The Shaped Sonic Boom Demonstration (SSBD) flight-test program used a modified F-5E aircraft to demonstrate substantial boom reduction through special re-contouring of an existing aircraft. Extensive airborne sampling tests were performed on both the baseline F-5E (Ref. 8) and SSBD aircraft (Ref. 9), providing a wealth of unique, high quality, and thoroughly documented data.^{31–36} Figure 15 shows both the baseline F-5E geometry, and F-5E geometry with SSBD modifications. The geometry includes such features as active engine inlets, Electronics Cooling System (ECS) inlets, and jet exhaust. The surface discretization contains 1.4 million triangles for the SSBD, and 1.0 million for the baseline F-5E.

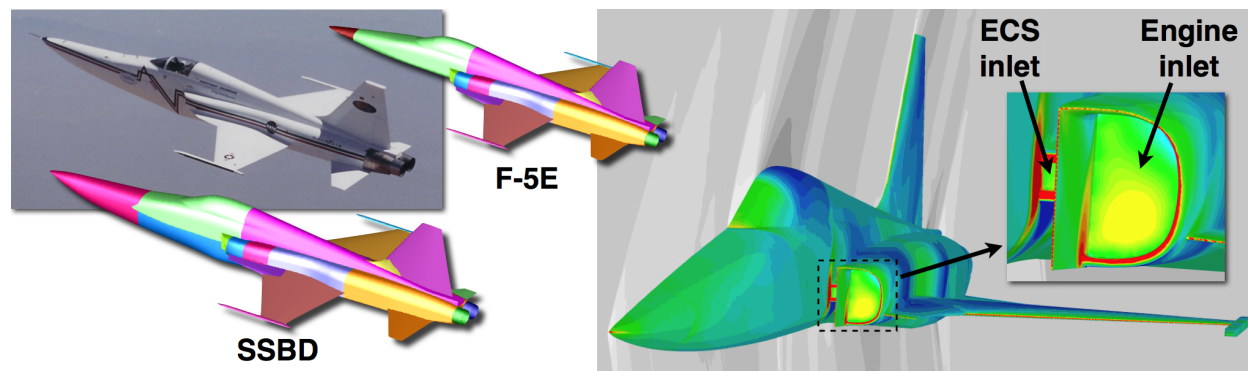
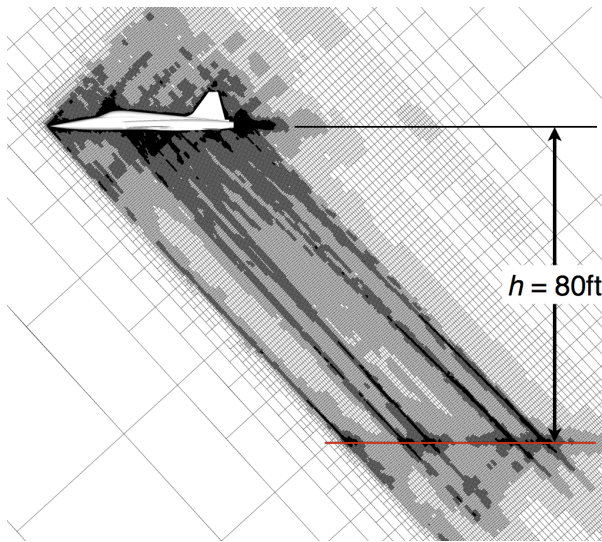


Figure 15. Computational surface models of the F-5E and SSBD aircraft with active engine inlet, ECS inlet and exhaust nozzles; surface discretizations contain 1.0M and 1.4M triangles, respectively. ECS and engine inlet locations indicated in the right panel

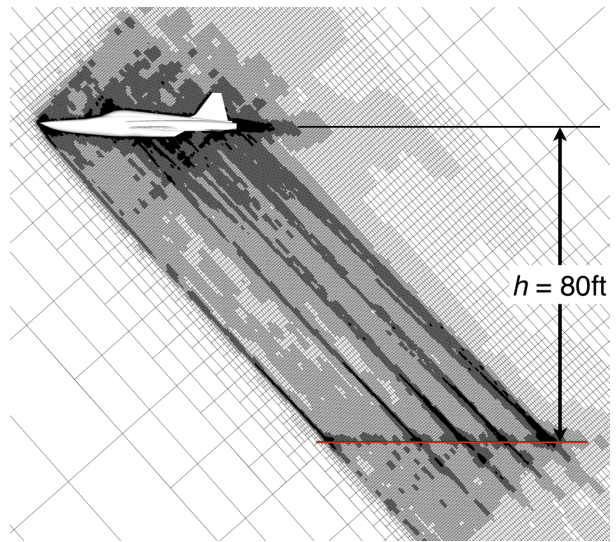
We start with a comparison of the near-field pressure signatures produced by the F-5E and SSBD aircraft. Simulation conditions are similar to flight test, with a freestream Mach number of 1.4, $C_L = 0.088$ (at $\alpha = 0.84$) for the F-5E, and $C_L = 0.084$ (at $\alpha = 1.72$) for the SSBD. The engine inlet and nozzle mass flow rates are 58.4 lb/s each, and the mass flow rate for the ECS is 0.824 lb/s. The grid is rotated 48.5° away from the Cartesian axes. The pressure sensor is located 80 ft below each aircraft, roughly approximating the location of the flight data. The far-field boundaries are located 600ft away from the body, and a symmetry plane is placed at $z = 0$. A mesh cell aspect ratio of 2 is used. Starting grids contain 23,985 and 26,469 cells for the F-5E and SSBD, respectively. An error tolerance of 0.01 is specified, and both body forces and pressure sensor are included in the target functional.

The final F-5E mesh, containing 11 million cells, is shown in Fig. 16(a), while that of the SSBD, containing 9.2 million cells, is shown in Fig. 16(b). Mach contours in the flowfield and pressure coefficient (C_p) on the body are shown in Fig. 16(c) for the F-5E and Fig. 16(d) for the SSBD. Pressure signals measured at the sensor are shown for the F-5E in Fig. 16(e) and for the SSBD in Fig. 16(f). Both sensors contain roughly 700 points along the sensor. The result of boom shaping is clearly evident in the SSBD signal, with a dramatically lower lift-induced shock. As also observed in the experimental data and CFD validation of Ref. 9, the bow shock strength increases relative to the baseline aircraft.

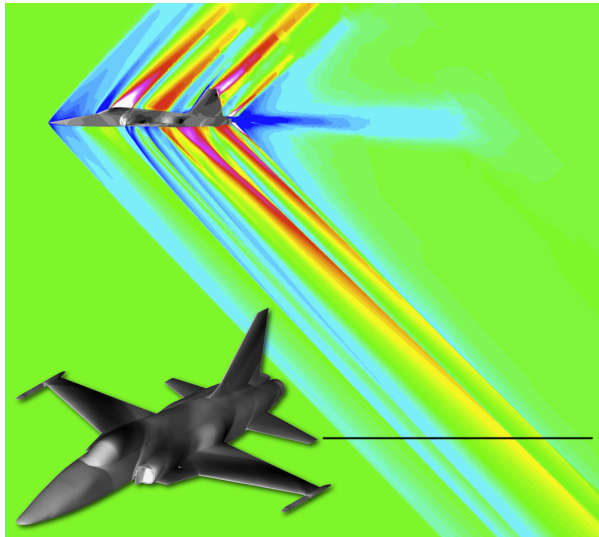
Finally, a preliminary comparison with a near-field pressure signal measured during flight test of the F-5E is presented. The post-processed flight test data indicates substantial peak-to-peak deviation in the vertical and transverse directions of the probing vehicle flight path. As emphasized in Ref. 9, this variation needs to be carefully accounted for to obtain good agreement with experimental values. In this preliminary comparison, we approximate the actual flight path taken by the “Signature 47” test (Ref. 8) using a two-segment sensor as sketched in Fig. 17(a). The pressure signal predicted by the adapted mesh is shown in Fig. 17(b). The experimental data (reproduced here from Ref. 8 with permission) is shown in Fig. 17(c). In addition to actual signal and flight path data, the active boundary conditions are an area that requires further attention. At this time, the mass flow rate is slightly too low for the inlet, and the nozzle stagnation conditions need to be refined to account for a thrust deficit. Nevertheless, we note that the overall length scale, shock locations and shock strengths show remarkably good agreement with the experimental data despite the nascent state of these results.



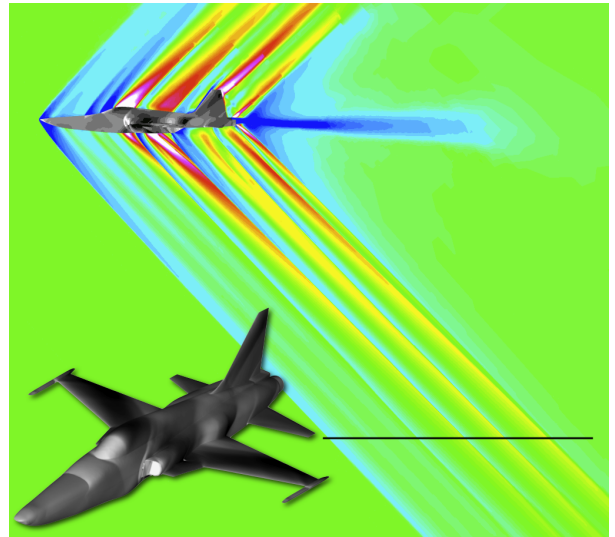
(a) F-5E adapted mesh; 11M cells



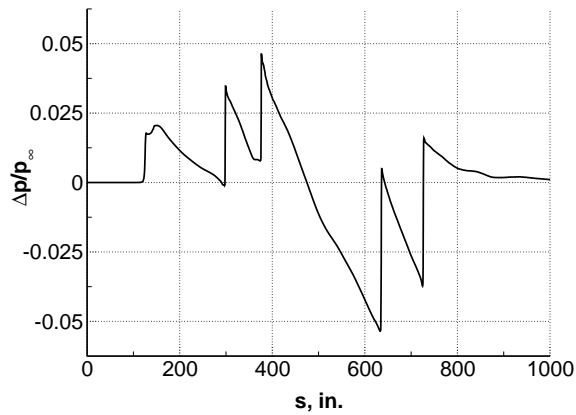
(b) SSBD adapted mesh; 9.2M cells



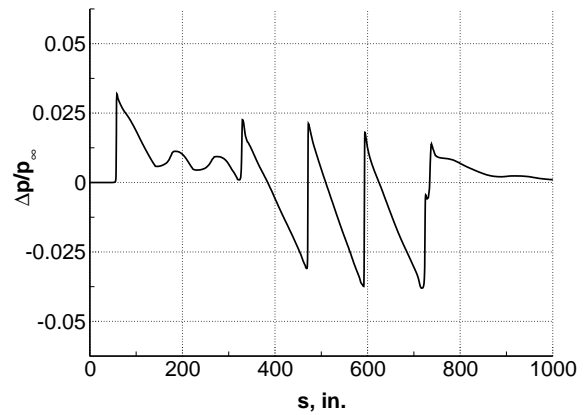
(c) F-5E flowfield Mach and surface C_p contours; $C_L = 0.088$



(d) SSBD flowfield Mach and surface C_p contours; $C_L = 0.084$

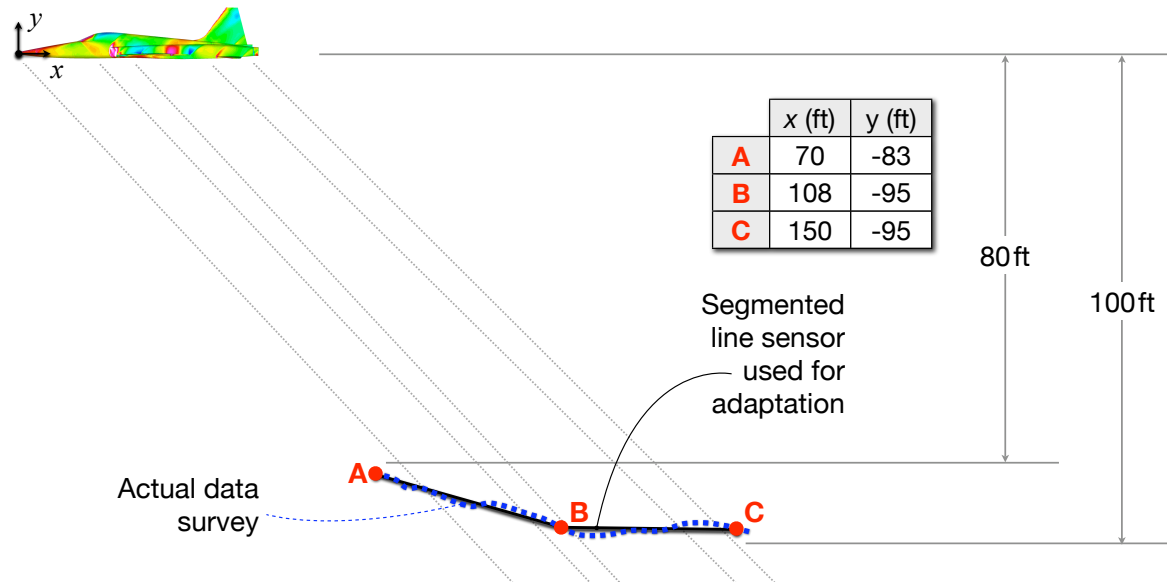


(e) F-5E off-body pressure signal measured on adapted mesh; 707 points along sensor

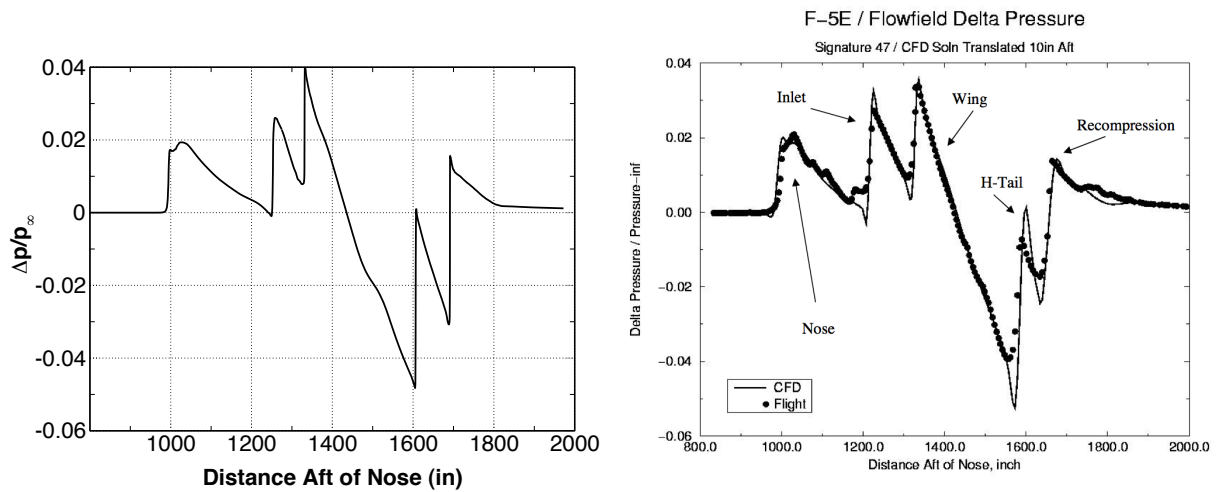


(f) SSBD off-body pressure signal measured on adapted mesh; 730 points along sensor

Figure 16. Comparison of adaptation results for F-5E and SSBD geometries. $M_\infty = 1.4$, $h = 80\text{ft}$, Mach contour range: $1.25(\text{blue}) \leq M_\infty \leq 1.55(\text{white})$, C_p contour range: $-0.3(\text{black}) \leq M_\infty \leq 0.3(\text{white})$



(a) F-5E probing flight path (from Ref. 8) and adaptation sensor geometry and location



(b) Pressure signal predicted on segmented sensor using mesh adaptation; 798 points along sensor

(c) Plot of experimentally sampled and CFD predicted near-field pressure signal for F-5E aircraft reproduced from Ref. 8 with permission

Figure 17. Comparison with experimental data of adaptation-predicted F-5E near-field pressure signal. $M_\infty = 1.4$, sensor location as indicated. Experimental data from Ref. 8, Signature 47

V. Conclusion

An adjoint-based mesh adaptation method was used to automatically develop volume grids tailored to the accurate prediction of pressure signals in the near-field of a body in supersonic flow. A refinement strategy appropriate for field functionals was coupled with grid alignment and cell stretching techniques to substantially reduce mesh densities required for accurate signal prediction.

The effectiveness of this adaptation methodology was examined using two test cases. Its fundamental capability in three dimensions was demonstrated on a trio of axisymmetric bodies, each producing unique signal forms, at a range of Mach numbers and offset distances. Simultaneous adaptation to body and field functionals was demonstrated on a wing-body at various lifting conditions. For both axisymmetric and wing-body test cases, results are validated against available experimental data, and agreement is shown to be excellent. The efficiency of the adaptation process is such that adapted meshes can be produced in 80 minutes on a conventional desktop PC. Finally, very promising results that compare favorably with flight test data are shown for real-world configurations using complex surface discretizations derived from highly detailed CAD surfaces.

Having demonstrated this robust, automated and rapid tool for prediction of near-field pressure signals using an Euler flow solver, we hope to motivate its use in conceptual design studies of future supersonic aircraft.

Acknowledgments

The authors gratefully acknowledge support from NASA grant NNX07AN01G, and contract NNA06BC19C. We wish to thank David Graham and Joseph Pawlowski (Northrop Grumman Corporation) for kindly providing ISSM and SSBD surface models and flight test data. We also wish to thank Arsenio-Cesa Dimanlig (ELORET Corporation) for sharing his expertise and enabling the translation of these surface models to simulation geometry.

References

- ¹Rodriguez, D. L. and Sturdza, P., "A Rapid Geometry Engine for Preliminary Aircraft Design," *44th AIAA Aerospace Sciences Meeting and Exhibit*, AIAA-2006-0929, Reno, Nevada, Jan. 2006.
- ²Sturdza, P., "Extensive Supersonic Natural Laminar Flow on the Aerion Business Jet," *45th AIAA Aerospace Sciences Meeting and Exhibit*, AIAA-2007-685, Reno, Nevada, Jan. 2007.
- ³Alonso, J. J., Kroo, I. M. and Jameson, A., "Advanced Algorithms for Design and Optimization of Quiet Supersonic Platforms," *40th AIAA Aerospace Sciences Meeting and Exhibit*, AIAA-20020144, Reno, Nevada, Jan. 2002.
- ⁴Pawlowski, J., Graham, D., Boccadoro, C., Coen, P. and Maglieri, D., "Origins and Overview of the Shaped Sonic Boom Demonstration Program," *43rd AIAA Aerospace Sciences Meetings and Exhibit*, AIAA-2005-5, Reno, Nevada, Jan. 2005.
- ⁵Simmons, F. and Freund, D., "Morphing Concept for Quiet Supersonic Jet Boom Mitigation," *43rd AIAA Aerospace Sciences Meeting and Exhibit*, AIAA-2005-1015, Reno, Nevada, Jan. 2005.
- ⁶Rodriguez, D., "Propulsion/Airframe Integration and Optimization on a Supersonic Business Jet," *45th AIAA Aerospace Sciences Meeting and Exhibit*, AIAA-2007-1048, Reno, Nevada, Jan. 2007.
- ⁷Dornheim, M. A., "Will Low-Boom Fly?" *Aviation Week & Space Technology*. Vol. 163, no. 18, pp. 68, 69. 7, Nov. 2005.
- ⁸Meredith, K. B., Dahlin, J. H., Graham, D. H., Malone, M. B., Haering, E. A., Jr., Page, J. A., and Plotkin, K. J., "Computational Fluid Dynamics Comparison and Flight Test Measurement of F-5E Off-Body Pressures," *43rd AIAA Aerospace Sciences Meeting and Exhibit*, AIAA-2005-0006, Reno, Nevada, Jan. 2005.
- ⁹Haering, E. A. Jr., Murray, J. E., Purifoy, D. D., Graham, D. H., Meredith, K. B., Ashburn, C. E., and Stucky, M., "Airborne Shaped Sonic Boom Demonstration with Computational Fluid Dynamics Comparisons", *43rd AIAA Aerospace Sciences Meeting and Exhibit*, AIAA-2005-0009, Reno, Nevada, Jan. 2005.
- ¹⁰Ozcer, I. A., and Kandil, O. A., "FUN3D / OptiGRID Coupling for Unstructured Grid Adaptation for Sonic Boom Problems," *46th AIAA Aerospace Sciences Meeting and Exhibit*, AIAA-2008-61, Reno, Nevada, Jan. 2008.
- ¹¹Jones, W. T., Nielsen, E. J. and Park, M. A., "Validation of 3D Adjoint Based Error Estimation and Mesh Adaptation for Sonic Boom Prediction," *44th AIAA Aerospace Sciences Meeting and Exhibit*, AIAA-2006-1150, Reno, Nevada, Jan. 2006.
- ¹²Nemec, M., Aftosmis, M. J. and Wintzer, M., "Adjoint-Based Adaptive Mesh Refinement for Complex Geometries," *46th AIAA Aerospace Sciences Meeting and Exhibit*, AIAA-2008-0725, Reno, Nevada, Jan. 2008.
- ¹³Aftosmis, M.J., Berger, M.J. and Melton, J.E., "Robust and Efficient Cartesian Mesh Generation for Component-Based Geometry." *AIAA Journal* 36(6):952-960, Jun. 1998.
- ¹⁴Fidkowski, K. J. and Darmofal, D. L., "Output-based Adaptive Meshing Using Triangular Cut Cells," *MIT Aerospace Computational Design Laboratory Report TR-06-2*, 2006.
- ¹⁵Park, M. A., and Darmofal, D. L., "Output-Adaptive Tetrahedral Cut-Cell Validation for Sonic Boom Prediction," *26th AIAA Applied Aerodynamics Conference*, AIAA-2008-6595, Honolulu, Hawaii, Aug. 2008.

- ¹⁶Nemec, M. and Aftosmis, M. J., "Adjoint Error Estimation and Adaptive Refinement for Embedded-Boundary Cartesian Meshes," AIAA-2007-4187, Miami, Florida, Jun. 2007.
- ¹⁷Thomas, C. L. "Extrapolation of Wind-Tunnel Sonic Boom Signatures without Use of a Whitham F-function" *NASA SP-255*, pp. 205-217, 1970.
- ¹⁸Plotkin, K. J., Grandi, F., "Computer Models for Sonic Boom Analysis: PCBoom4, CABoom, BooMap, CORBoom," *Wyle Report WR 02-11*, Jun. 2002.
- ¹⁹van Leer, B., "Flux-Vector Splitting for the Euler Equations," *ICASE Report 82-30*, Sep. 1982.
- ²⁰Aftosmis, M. J., Berger, M. J., and Adomavicius, G., "A Parallel Multilevel Method for Adaptively Rened Cartesian Grids with Embedded Boundaries," AIAA-2000-0808, Reno, Nevada, Jan. 2000.
- ²¹Aftosmis, M. J., Berger, M. J., and Murman, S. M., "Applications of Space-Filling-Curves to Cartesian Methods for CFD," AIAA-2004-1232, Reno, Nevada, Jan. 2004.
- ²²Berger, M. J., Aftosmis, M. J., and Murman, S. M., "Analysis of Slope Limiters on Irregular Grids," AIAA-2005-0490, Reno, Nevada, Jan. 2005.
- ²³Venditti, D. A. and Darmofal, D. L., "Grid Adaptation for Functional Outputs: Application to Two-Dimensional Inviscid Flow," *Journal of Computational Physics*, Vol. 176, pp. 4069., 2002.
- ²⁴Nemec, M., Aftosmis, M. J., Murman, S. M., and Pulliam, T. H., "Adjoint Formulation for an Embedded-Boundary Cartesian Method," AIAA-2005-0877, Reno, Nevada, Jan. 2005.
- ²⁵Nemec, M., and Aftosmis, M. J., "Adjoint Error Estimation and Adaptive Refinement for Embedded-Boundary Cartesian Meshes," AIAA Paper 2007-4187, Miami, FL, June 2007.
- ²⁶Moschetta, J.-M., and Gressier, J., "The sonic point glitch problem: A numerical solution", *Lecture Notes in Physics*, Vol. 515, pp. 403-408., 1998.
- ²⁷Carlson, H. W., Mack R. J., Morris O. A., "A Wind tunnel Investigation of the Effect of Body Shape on Sonic Boom Pressure Distributions," *NASA TN D-3106*, 1965.
- ²⁸Hunton, L. W., Hicks, R. M., and Mendoza, J. P., "Some Effects of WingPlanform on Sonic Boom," *NASA TN D-7160*, Jan. 1973.
- ²⁹Cliff, S. E., and Thomas, S. D., "Euler/Experiment Correlations of Sonic Boom Pressure Signatures", *Journal of Aircraft*, Vol. 30, No. 5, Sep.-Oct. 1993
- ³⁰Aftosmis, M. J., Delanaye, M., and Haimes, R., "Automatic Generation of CFD-Ready Surface Triangulations from CAD Geometry," AIAA-1999-0776, Reno, Nevada, Jan. 1999.
- ³¹Graham, D. H., Dahlin, J. H., Page, J. A., Plotkin, K. J., and Coen, P. G., "Wind Tunnel Validation of Shaped Sonic Boom Demonstration Aircraft Design," *43rd AIAA Aerospace Sciences Meeting and Exhibit*, AIAA-2005-0007, Reno, Nevada, Jan. 2005.
- ³²Graham, D. H., Dahlin, J. H., Meredith, K. B., and Vadnais, J., "Aerodynamic Design of Shaped Sonic Boom Demonstration Aircraft," *43rd AIAA Aerospace Sciences Meeting and Exhibit*, AIAA-2005-0008, Reno, Nevada, Jan. 2005.
- ³³Plotkin, K., Haering, E., Murray, J., Maglieri, D., Salamone, J., Sullivan, B., and Schein, D., "Ground Data Collection of Shaped Sonic Boom Demonstration Aircraft Pressure Signatures," *43rd AIAA Aerospace Sciences Meeting and Exhibit*, AIAA-2005-0010, Reno, Nevada, Jan. 2005.
- ³⁴Plotkin, K., Martin, M. L., Maglieri, D., Haering, E., and Murray, J., "Pushover Focus Booms From the Shaped Sonic Boom Demonstrator," *43rd AIAA Aerospace Sciences Meeting and Exhibit*, AIAA-2005-0011, Reno, Nevada, Jan. 2005.
- ³⁵Morgenstern, J. M., Arslan, A., Pilon, A., Lyman, V., and Vadyak, J., "F-5 Shaped Sonic Boom Demonstrators Persistence of Boom Shaping Reduction Through Turbulence," *43rd AIAA Aerospace Sciences Meeting and Exhibit*, AIAA-2005-0012, Reno, Nevada, Jan. 2005.
- ³⁶Kandil, O. A., and Bobbitt, P. J., "Comparison of Full-Potential-Equation, Propagation-Code Computations with Measurements from the F-5 Shaped Sonic Boom Experiment Program," *43rd AIAA Aerospace Sciences Meeting and Exhibit*, AIAA-2005-0013, Reno, Nevada, Jan. 2005.